

https://doi.org/10.1038/s44310-025-00053-w

Hyperbolic polaritons in twisted β-Ga₂O₃

Check for updates

Yuan Zheng¹, Yali Zeng², Yidan Hu¹, Lu Liu³, Zhigao Dai³ & Huanyang Chen¹⊠

Hyperbolic polaritons (HPs) are essential for integrated photonics due to their directional propagation and strong field confinement. While most research focuses on in-plane light behavior, the out-of-plane features of HPs remain underexplored. In this work, we theoretically predict a novel light coupling mechanism in twisted β -Ga $_2$ O $_3$ bilayers, involving both surface and volume HPs. As the twist angle increases, the polaritons merge, transitioning from a "four-wing" to a "two-wing" state, accompanied by changes in the iso-frequency contours (IFCs). This shift in dispersion and field distribution results from the interaction between surface and volume HPs, wherein they exchange energy and modify their vertical locality. We also introduce a method for analyzing mode interactions via wavevector collinearity. Our work extends twistronics to control the vertical locality of polaritons, enabling new possibilities for sub-wavelength light manipulation with applications in super-resolution imaging, nanophotonics, and compact photonic devices.

Phonon polaritons, quasiparticles resulting from the interaction between photons and lattice vibrations¹⁻⁵, have garnered significant interest due to their low loss and intense field confinement. Recently, van der Waals (vdW) materials have been shown to support phonon polaritons, which has attracted considerable attention. For instance, elliptical and hyperbolic polaritons have been observed in single-layer α-MoO₃, attributed to the inplane anisotropy of the materials⁵. It is also observed that two different modes of hyperbolic polaritons (HPs)—a surface mode and a volume mode —coexist in α -MoO₃⁶. Researchers have also explored similar properties in other van der Waals materials, demonstrating various polaritonic behaviors in WTe₂^{7,8}, α -V₂O₅⁹, ATeMoO₆¹⁰, h-BN^{2,11,12}, and $LiV_2O_5^{13}$. The primary research focus on the manipulation of light at sub-wavelength scale. So far, several techniques have been used, including adjusting the frequency of incident light^{2,5,14,15}, varying material thickness¹³, cutting crystals in different directions 16,17, selecting diverse substrates 18, and altering the isotopic enrichment of materials^{15,19}. While these approaches modulate the loss, wavelength, and distribution of polaritons, they do not address the crystal lattice, a fundamental determinant of crystal properties. A novel approach was further introduced¹⁸ by stacking slabs of α-MoO₃ at multiple angles, leading to a topological transition in dispersion from hyperbolic to elliptical. Since atomic arrangement is closely linked to the band structure and interlayer coupling in vdW materials, altering the lattice's periodicity and symmetry through rotation^{18,20,21} enables phenomena like canalization^{22,21} and topological transitions of polaritons^{21,24,25}, with a new concept termed "twistronics" $^{26-28}.$ However, many vdW materials, such as $\alpha\text{-MoO}_3$ and $\alpha\text{-}$ V₂O₅, exhibit high symmetry of crystal, affecting the dispersion of their permittivity tensors²⁹⁻³¹. This symmetry restricts permittivity variation, limiting polariton excitation to specific combinations of permittivity, such as in-plane anisotropy with positive out-of-plane components and in-plane isotropy with negative out-of-plane components. Consequently, only one type of polaritons, whether surface, volume³², or ghost modes¹⁷, could be typically excited. Therefore, the coupling and topological transition involve only polaritons with the same out-of-plane distribution, excluding the manipulation of vertical locality, and affect only the in-plane field distributions.

In contrast, crystals with lower symmetry, like $CdWO_4^{33}$ and β - $Ga_2O_3^{34,35}$, can exhibit more varied frequency-dispersive dielectric permittivity. β - Ga_2O_3 , a monoclinic crystal, supports hyperbolic shear polaritons. Unlike orthorhombic crystals, the dispersion of its permittivity is less regular, allowing for the identification of more frequencies where permittivity differs significantly across directions. β - Ga_2O_3 provides us a great platform to study the manipulation of polaritons, and give us a deeper insight into the relationship of crystal structure and the feature of polaritons.

In this study, by stacking β -Ga₂O₃ slabs of equal thickness, we observe the coexistence of the fundamental mode (M₀) and the first higher order mode (M₁) at multiple frequencies. As the upper slab rotates, the electric field transitions from a "four-wings" to a "two-wings" pattern. Following the preceding methodology³⁶, we derive a dispersion model for the bilayer structure. To address limitations in previous models, our analytical approach incorporates the influence of out-of-plane permittivity, enabling the distinction between surface and volume modes. Additionally, we examine the vertical electric fields of polaritons and reveal a correlation between the vertical confinement of polaritons and the parity of the electric

¹Department of Physics, Xiamen University, Xiamen, 361005, China. ²Key Laboratory of Light Field Manipulation and Information Acquisition Ministry of Industry and Information Technology and School of Physical Science and Technology, Northwestern Polytechnical University, Xi'an, China. ³Engineering Research Center of NanoGeomaterials of Ministry of Education, Faculty of Materials Science and Chemistry, China University of Geosciences, Wuhan, 430074, China.

≥ e-mail: kenyon@xmu.edu.cn

field. Our findings extend the understanding of polariton coupling by revealing interactions between polaritons with distinct vertical localities.

Results

The bilayer β-Ga₂O₃ structure and numerical simulations

We constructed a twisted bilayer structure, where both layers of β-Ga₂O₃ are of equal thickness (Fig. 1a). For simplicity, we have chosen air as both the substrate and superstrate. However, low-loss materials with a minimal real permittivity in the range of 705-730 cm⁻¹ would also be suitable as the substrate. The slabs are assumed to be infinite in-plane. Crystal directions [100] and [010] were designated as the x and z axes, respectively. Given the monoclinic symmetry of β -Ga₂O₃^{34,35}, the crystal direction [001] is orthogonal to [010] and forms an angle of 103.7° with [100]. To simplify the coordinate system, we selected the direction that forms a right-handed coordinate with the x and z axes as the y-axis. The twist angle between the two layers is denoted as θ . Owing to the low symmetry of β -Ga₂O₃, its permittivity tensor exhibits significant differences compared to orthorhombic crystals like α-MoO₃ ^{37,38}, especially in the presence of non-diagonal elements (Fig. 1b). The permittivity along the principal axes differ significantly in their dispersion, allows greater flexibility for subwavelength light control^{29,31}.

Within the Reststrahlen band of β -Ga₂O₃, HPs are excited when the permittivity components along the x and y directions exhibit opposite signs. To support additional modes in the slabs, we maintain a uniform thickness of 400 nm for β -Ga₂O₃ in the simulation. Notably, in the monoclinic crystal β -Ga₂O₃, the excitation of HPs is governed not only by the sign of the inplane dielectric permittivity values but also by the out-of-plane permittivity²⁹. When the in-plane components have opposite signs and the real part of the out-of-plane permittivity is negative, two branches of HPs with different orientations are simultaneously excited within the plane. We

perform the simulation by finite element software COMSOL Multiphysics, both the real and imaginary parts of the permittivity tensor is considered in the modeling, and the bilayer β-Ga₂O₃ is sandwiched by air. The whole model is surrounded by Perfect Matched Layers (PML), therefore most of the scattering light can be absorbed and modeling the case where light propagates over an infinite distance without reflection on the edges. Figure 2 exhibits the simulated field at $\theta = 0^{\circ}$, 45°, and 90° for a fixed frequency of 714 cm⁻¹. Numerical simulations reveal two hyperbolic polariton waveforms —a smaller one and a larger one—coexisting within the structure (Fig. 2a). The fast Fourier transform (FFT) of Re(E₇) reveals two contiguous hyperbolas (Fig. 2d), and E_z is the z component of the electric field. We refer to this phenomenon, where two branches of HPs coexist, as the "four-wings" state. In contrast, when only one branch of HPs is present, we describe it as the "two-wings" state. Upon rotating the upper layer of β -Ga₂O₃, the smaller polariton diminishes (see Supplementary Information, Section 2). The wavelength and propagation distance of the larger polariton also change as the twist angle θ increases (Fig. 2b, c). Hence, the merging of HPs is accompanied by increased loss, suggesting energy redistribution within the β-Ga₂O₃ waveguide. While the momentum shifts of the larger polariton indicate variations in dispersion, demonstrating coupling between the polaritons. The changes in the dispersion align with the alterations in the field distribution (Fig. 2e, f). Throughout this process, the polaritons retain a hyperbolic shape, which contrasts with previously observed transitions where the field pattern evolves from an open hyperbola to a closed ellipse^{6,39}.

The dispersion relations of polaritons

To elucidate the underlying mechanism of this phenomenon, we need to develop a suitable dispersion model to better capture the coupling and redistribution of polaritons during rotation. It is well established that the wavelength of polaritons is significantly smaller than that of incident

Fig. 1 | Schematic plot of the bilayer β -Ga₂O₃ and β -Ga₂O₃'s frequency-dispersive permittivity. a Twisted stacks of β -Ga₂O₃ with a thickness of d. The superstrate and substrate are air. Direction [001] is within the x-y plane but is not orthogonal to the x-axis [001]. b The components of permittivity tensor of β -Ga₂O₃.

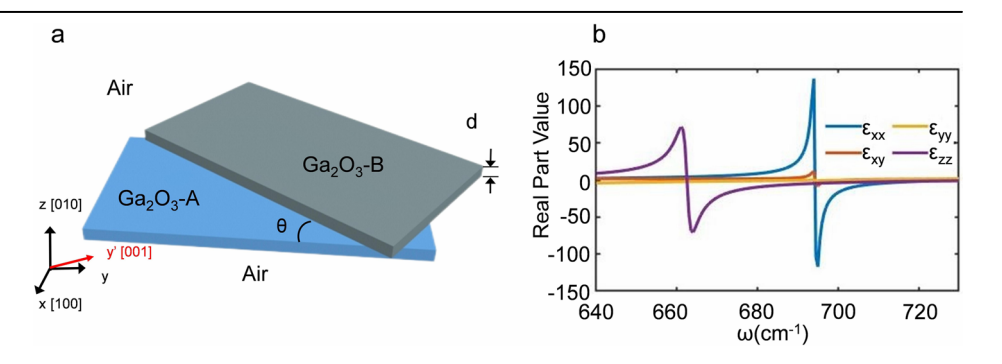
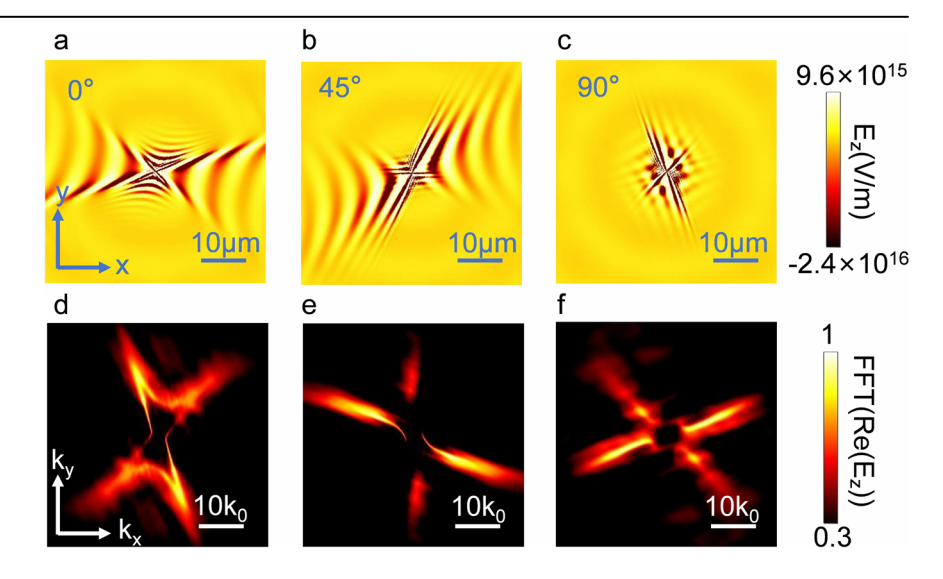


Fig. 2 | The transition of HPs with the rotation of the upper slab. a The field distribution at $\theta=0^\circ$ and the corresponding Fourier spectrum (d). Two distinct HPs coexist. b, c The field distribution at $\theta=45^\circ$ and $\theta=90^\circ$, and the corresponding Fourier spectrum (e, f), respectively. HPs gradually merge while retaining their hyperbolic character.



light^{12,40}. Previous studies have proposed a method for modeling the dispersion relation based on the birefringence characteristics of crystals, identifying the two extraordinary waves in a biaxial birefringent crystal as "o" and "e" polarizations³⁶. In isotropic cases, the eigenvectors of o and e waves degenerate into those of "s" and "p" waves, indicating the continuity of electromagnetic field at the interface between vdWs materials and air. However, when analyzing two stacked layers of β-Ga₂O₃, the coefficient matrix derived from this method proves difficult to simplify. Consequently, we are unable to obtain an simplified solution akin to that in previous works, which separates each mode by orders. Another approach mentioned in prior studies treats material layers as planes with no thickness and employs conductivity (σ) in the calculations^{5,18,21}. However, this method is unsuitable for our case as it only considers the in-plane permittivity components and neglects the out-of-plane permittivity. The out-of-plane permittivity, however, significantly influences both the distribution and vertical localities of polaritons^{6,29}.

Therefore, a novel approach is required to analyze the dispersion relation in bilayer $\beta\text{-}Ga_2O_3$. The "four wings" primarily result from the real part of the permittivity tensor, as the imaginary part is significantly smaller by comparison. Therefore, the imaginary component of the permittivity tensor can be neglected in the subsequent calculations. Starting from the source-free Maxwell equations, we represent the plane waves in the slabs by the eigenvectors $|o\rangle$ and $|e\rangle$, while the plane waves in the substrate and superstrate are represented by $|s\rangle$ and $|p\rangle$,

$$|e_{o}\rangle = \frac{1}{q} \begin{pmatrix} e_{ox} \\ e_{oy} \\ e_{oz} \end{pmatrix}, |e_{e}\rangle = \frac{1}{q} \begin{pmatrix} e_{ex} \\ e_{ey} \\ e_{ez} \end{pmatrix}, |s\rangle = \frac{1}{q} \begin{pmatrix} -q_{y} \\ q_{x} \\ 0 \end{pmatrix}, |p\rangle = \frac{1}{q} \begin{pmatrix} q_{x} \\ q_{y} \\ \frac{q^{2}}{\mp iq_{z}} \end{pmatrix}$$
(1)

where $q_i = (i = x, y, z)$ are components of normalized wavevectors, and $e_{ij}(i = o, e; j = x, y, z)$ denote the components of electric fields in crystal, as detailed in Eq. S10, Supplementary Information, Section 1. We can calculate the electric field in each region of the structure and express the fields in each layer as a superposition of plane waves (see Supplementary Information, Section 1 for details).

The tangential components of both the electric field intensity E and the magnetic field intensity H are continuous at the boundary. Consequently, we introduce the in-plane sub-vectors of E's eigenvectors, denoted $|\xi_n\rangle$, and derive the sub-vectors of H, denoted $|\xi_n\rangle_{\pm}$, from the relation $H_t = e_z \times \mathbf{q}_i \times E$. n=1,2,3,4 represent the regions in the model, and $\xi=o,e,s,p$. The dispersion equations are derived from the continuity of the field (see Eq. S15, Supplementary Information, Section 1). To simplify these equations, we adopt the "large k" approximation, where $k\gg k_0$, with k and k_0 denoting the polaritonic and free-space wavevectors, respectively. Under this assumption, the boundary condition does not apply to the o-wave within the material or the s-wave outside it, allowing us to focus exclusively on the e- and p-waves. The equations are multiplied with bravectors $\langle p|$, simplified using Gaussian elimination, and are expressed in matrix form as follows:

Where k_z is the wavenumber along z-axis. For the equations to have non-zero solutions, the determinant of the coefficient matrix must be zero. After the simplification of the matrix, we have the dispersion equation by expand its determinant:

$$\begin{split} & \sinh{(k_{2ez}d)}[q_{3ez}(q^2\varepsilon_1\varepsilon_4+q_{2ez}^2\varepsilon_{zz}^2) \cosh{(k_{3ez}d)}+q(q_{3ez}^2\varepsilon_1+iq_{2ez}^2\varepsilon_4)\varepsilon_{zz} \sinh{(k_{3ez}d)}]+\\ & q_{2ez} \cosh{(k_{2ez}d)}[qq_{3ez}(\varepsilon_1+\varepsilon_4)\varepsilon_{zz} \cosh{(k_{3ez}d)}+(iq^2\varepsilon_1\varepsilon_4+q_{3ez}^2\varepsilon_{zz}^2) \sinh{(k_{3ez}d)}]=0. \end{split}$$

By Eq. (3) we obtain the iso-frequency contours (IFCs), namely, the dispersion curves of polaritons (Fig. 3). Due to the periodic nature of the dispersion equation, the IFCs display modes of different orders together. These IFCs represent potential guided modes in k-space, but only the lowerorder modes, which experience less loss, can propagate in real space. In contrast, higher-order modes, exhibiting greater loss, do not appear in the electric field. Since the IFCs of higher-order modes tend to occur at larger k-space coordinates, we limit the plotting range to focus on the lower-order modes associated with polaritons observed in the simulated electric fields. The similarity between the Fourier spectrums and the dispersion validates our model (see Supplementary Information, Section 2). The IFCs of singlelayer β-Ga₂O₃ illustrate that the electric dipole simultaneously excites two types of modes in the crystal: volume modes and surface modes (see Supplementary Material, Section 3). Surface modes propagate over extended distances in-plane yet decay rapidly along the out-of-plane direction. These modes are essentially evanescent waves localized at the interface between the two-dimensional materials and air, characterized by $Im[k_z] >> Re[k_z]^{16,41}$. In contrast, volume modes, which exhibit less decay along the out-of-plane direction, behave as harmonic waves that oscillate and transmit within the slab waveguide, with $Re[k_z] >> Im[k_z]^{42,43}$. Utilizing the distinct features of surface and volume modes, we obtain their IFCs from the imaginary and real parts of Eq. (2), respectively, and represent them with warm colors (red and yellow) for surface modes and cool colors (light and dark blue) for volume modes (Fig. 3). By comparing the IFCs of single-layer β-Ga₂O₃ with the obtained dispersion contours and the simulated fields, it is evident that the larger polariton in the field aligns with the fundamental mode (M_0) while the smaller one aligns with the first higher-order mode (M₁) (see Supplementary Material, Section 3). The former is a surface mode, while the latter is a volume mode, the two modes exhibit distinct vertical localities.

We first analyze the coupling between modes of the same order and vertical locality. As the rotation proceeds, the IFCs of M_0 continuously transform (see Supplementary Information, Section 2), driven by the hybridization of the two distinct surface modes. In contrast, the two M_1 modes do not couple. Only a pair of hyperbolic blue IFCs rotates, while the other remain stationary, with their hyperbolic shapes unchanged due to the absence of interaction between the M_1 modes.

However, examining the coupling between identical modes alone proves insufficient, it is essential to uncover the interactions between distinct modes. Unlike the interaction of identical modes, the coupling of different order modes does not lead to the fusion of iso-frequency contours (IFCs) like^{18,44}, as each IFC serves as an eigen solution of the dispersion equation (Eq. 2). Therefore, we need to find another solution to explain the coupling

$$\begin{pmatrix} -\langle p|p\rangle e^{ik_{1z}d} & \langle p|e_{2}\rangle e^{ik_{2ez}d} & \langle p|e_{2}\rangle e^{-ik_{2ez}d} & \overline{0} & 0 & 0 \\ 0 & \langle p|e_{2}\rangle & \langle p|e_{2}\rangle & -\langle p|e_{3}\rangle & -\langle p|e_{3}\rangle & 0 \\ 0 & 0 & 0 & \langle p|e_{3}\rangle e^{-ik_{3ez}d} & \langle p|e_{3}\rangle e^{ik_{3ez}d} & -\langle p|p\rangle e^{-ik_{4z}d} \\ 0 & -\langle p|p_{1}\rangle'_{+}e^{ik_{1z}d} & \langle p|e_{2}\rangle'_{+}e^{ik_{2ez}d} & \langle p|e_{2}\rangle'_{-}e^{-ik_{2ez}d} & 0 & 0 & 0 \\ 0 & \langle p|e_{2}\rangle'_{+} & -\langle p|e_{2}\rangle'_{-} & \langle p|e_{3}\rangle'_{+} & -\langle p|e_{3}\rangle'_{-} & 0 \\ 0 & 0 & \langle p|e_{2}\rangle'_{+}e^{-ik_{3ez}d} & \langle p|e_{3}\rangle'_{-}e^{ik_{3ez}d} & -\langle p|p_{4}\rangle'_{-}e^{-ik_{4z}d} \end{pmatrix} \begin{pmatrix} b_{1} \\ a_{2} \\ b_{2} \\ a_{3} \\ b_{3} \\ b_{4} \end{pmatrix} = 0.$$
 (2)

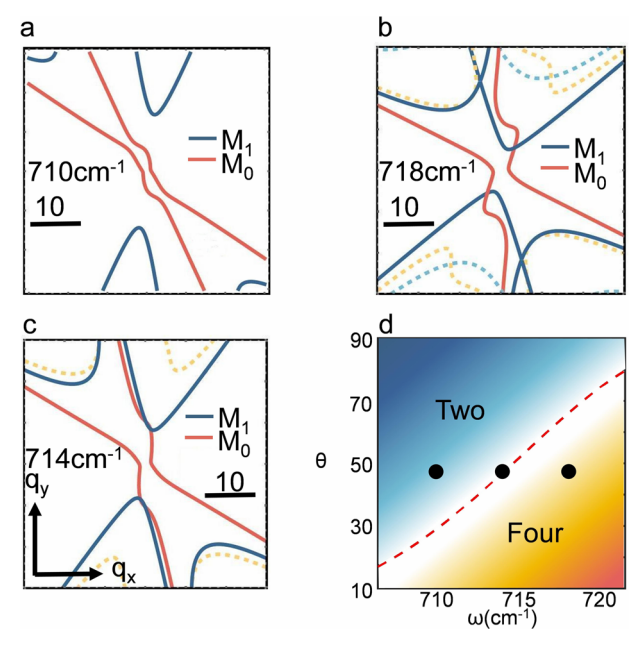


Fig. 3 | Analytical explanation of the transition from "two-wings" state to "fourwings" state. a IFCs at $\omega = 710 \text{ cm}^{-1}$, the red and bule curves are separated. b IFCs at $\omega = 718 \text{ cm}^{-1}$, the red and bule curves intersect. c IFCs at $\omega = 714 \text{ cm}^{-1}$, the red and bule curves are parallel to each other. d Relationship between the distribution of polaritons with the frequency ω and twist angle θ . The dashed line denotes the critical angle as a function of frequency. Black dots represent the chosen frequencies of the IFCs. The blue and orange regions represent cases in which the field distribution appears to be "two-wings" and "four-wings", respectively. The coordinates are the normalized wavevectors qx and qy, resulting in unitless scale bars. Dashed dispersion curves represent higher-order modes that do not exist in real space and are not involved in coupling, while solid curves denote modes present in the field. Yellow dashed curves indicate higher-order surface modes, and blue dashed curves represent higher-order volume modes. Red solid curves denote M₀, while the blue solid curves signify M1. The relative positioning of these curves illustrates the coupling between the two modes, greater collinearity of their wavevectors correlates with stronger interaction. The IFCs are plotted at the fixed angle of 47.5°, and are derived from the dispersion Eq. (3).

in the momentum space. Comparison of polariton dispersion with variations in the simulated fields reveals that the coupling between two distinct modes can be elucidated by the superposition of their wavevectors \mathbf{k} (see Supplementary Material, Section 2). The magnitude and orientation of **k** are closely linked to the light propagation. For points on the IFCs, the corresponding wavevectors are represented by their connection to the origin of the coordinates (O, $q_x = q_y = 0$). As the IFCs show, there are no collinear wavevectors for M_0 and M_1 at $\theta = 0$ (see Supplementary Material, Fig. S1a). However, as the upper slab rotates, collinear wavevectors \mathbf{k} of the two modes emerge, and simultaneously, the simulated field reveals the fusion of polaritons (see Supplementary Information, Section 2). The greater the collinearity between the wavevectors of M₀ and M₁, the more deeply they fuse. Ultimately, the IFCs reach a critical point where the surface mode transitions from intersecting the volume mode to becoming tangent or parallel, indicating complete overlap of the wavevector ranges for Mo and M₁. Compared to the electric field, this critical point corresponds precisely to the angle θ at which the smaller polariton vanishes, signaling the full integration of surface and volume modes. Thus we define the twist angle at which the red and blue curves are just tangent or parallel as the critical angle of transition between "four-wings" mode and "two-wings" pattern. Within the frequency range of 706 to 722 cm⁻¹;, the critical angle is positively correlated with frequency (Fig. 3d). At a fixed angle of 47.5°, we present IFCs at three frequencies—710 cm⁻¹ (Fig. 3a), 714 cm⁻¹ (Fig. 3c), and 718 cm⁻¹ (Fig. 3b)—corresponding to the black dots in Fig. 3d. It is evident that the red and blue curves are relatively far apart in the "two-wings" region at 710 cm⁻¹

(Fig. 3d), where all wavevectors of the volume mode have collinear counterparts in the surface mode (Fig. 3a). At 714 cm⁻¹, the two IFCs become parallel (Fig. 3c). However, at 718 cm⁻¹, the blue curves still intersect with the red, indicating that some wavevectors of the volume mode remain noncollinear with those of the surface mode (Fig. 3b). As a result, the polaritons retain a "four-wings" configuration, with the smaller volume mode persisting. Moreover, to verify the definition of the critical angle, we stack the IFCs of single-layer β-Ga₂O₃ at various angles (see Supplementary Information, Section 6). The curves of the two M₁s are precisely tangent at the critical angle of 47.5°, indicating that the collinearity between the wavevectors almost reaches its maximum at this angle, thereby confirming the validity of our analysis of coupling through k. Theoretical analysis reveals that the transition from "four-wings" state to "two-wings" state arises from the interaction between polaritons with distinct vertical localities. Compared to previous work¹⁴, this introduces a new dimension for polariton coupling.

Analysis of coupling from the perspective of vertical field distribution

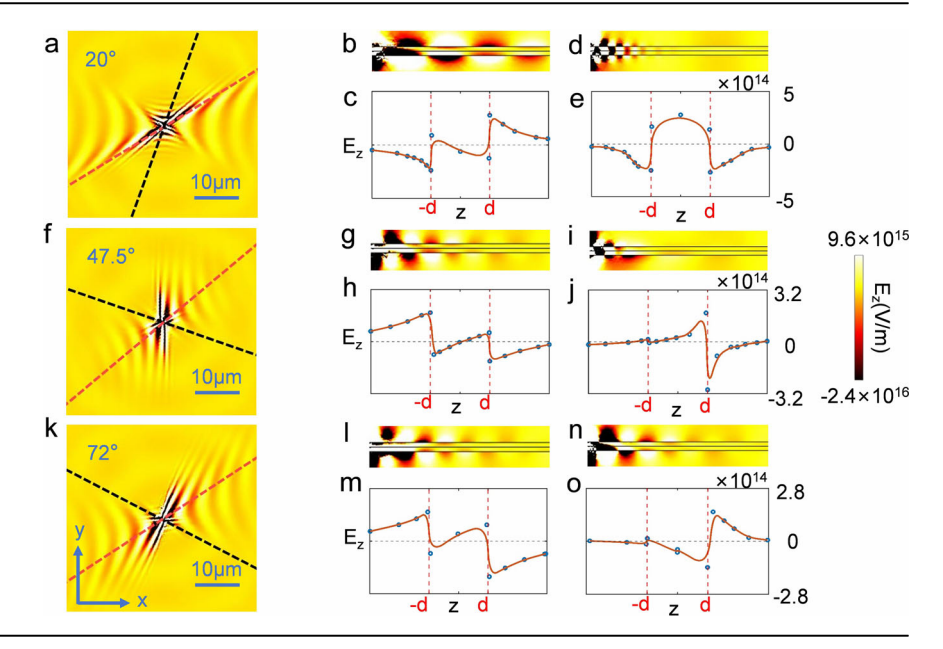
To further elucidate the surface-volume coupling during the rotation, we need to find out how the vertical localities of polariton change. If the modulus of the electric field intensity |E| peaks at the slab's center, the polariton is identified as a volume mode; if |E| reaches a local minimum, it is classified as a surface mode⁶. Some polaritons also exhibit intermediate characteristics between these two states. We begin with the case where the $\theta = 20^{\circ}$, sectioning the field in the direction where the two modes exhibit their largest amplitudes (Fig. 4a). For the volume mode, the cross profile reveals a distinct oscillatory pattern within the β-Ga₂O₃, represented by alternating light and dark pattern (Fig. 4d). Conversely, the surface mode produces a "hollow" region at the center, indicating that the surface polariton does not penetrate into the middle of the waveguide due to the large out-plane loss (Fig. 4b). This observation confirms the previous analysis of surface and volume characteristics (Fig. 3). As the twist angle θ approaches the critical angle of 47.5° (Fig. 4f), the propagation directions of the two modes gradually overlap, leading to their coupling. The behavior of the volume mode changes significantly (Fig. 4i), the corresponding E_z no longer reaches its maximum at z = 0 (Fig. 4j). The volume mode loses its intrinsic nature, signaling increased loss within the slab. At the same θ , Fig. 4g shows the vertical field distribution of the surface mode is also affected, featuring lower loss along the z-axis, suggesting the coupling between the volume and surface modes. As rotation continues (Fig. 4k-o), the fusion of the two modes becomes more pronounced. For the volume mode, the field within the material decreases, while the surface mode becomes more prominent inside the waveguide. However, the cross profiles and plots at $\theta = 72^{\circ}$ show little difference from those at $\theta = 47.5^{\circ}$, indicating that as θ reaches the critical angle, the two polaritons have nearly fully integrated, with the degree of fusion changing little with further increases in the angle between the slabs. Changes in the vertical field illustrate the overlap of surface and volume modes, confirming their interaction. It is also discovered that the wavelength of the surface mode decreases as the twist angle of the slabs increase.

Additionally, the z component of M_0 and M_1 exhibit distinct parities, as they belong to different orders. The E_z of M_1 exhibits even parity, with a mirror-symmetric electric field distribution about the line z=0 (Fig. 4e). In contrast, the E_z of M_0 displays a distribution akin to an odd function on either side of z=0 (Fig. 4c). This distinction allows us to observe the transition and coupling mechanisms of the polaritons not only through the intensity distribution of the modes but also through their symmetry. Comparing the distributions of E_z along z-axis, we can see both the M_0 and M_1 gradually lost their original parity, and both of them acquire some characters of each other (Fig. 4h, j, m, o).

Discussions

In conclusion, by stacking slabs of β -Ga₂O₃, we discover the coexistence of different order modes of two distinct vertical localities within a specific frequency range. Based on this, we reveal a novel coupling behavior of

Fig. 4 | Cross sections of the electric fields at $\omega = 714 \text{ cm}^{-1}$. a The electric field at $\theta = 20^{\circ}$. b, d The cross-sections of the surface and volume mode at $\theta = 20^{\circ}$, with their corresponding E_z distributions (c, e), respectively. The surface mode (M_0) exhibits odd parity, while the volume mode (M1) shows even parity. **f** The electric field at $\theta = 47.5^{\circ}$. **g**, **i** The crosssections of the surface and volume mode at $\theta = 47.5^{\circ}$, with their corresponding E_z distributions (**h**, **j**), respectively. **k** The electric field at $\theta = 72^{\circ}$. **l**, **n** The cross-sections of the surface and volume mode at $\theta = 72^{\circ}$, along with their corresponding E_z distributions (m, o), respectively. Blue dots in the plot represent the data, and the orange curves denote the results of fitting. As θ increases, the polaritons gradually gained more features of each other.



polaritons during rotation. Specifically, the coupling of the two modes increases the loss of the volume mode, while the surface mode acquires volume properties through this interaction. Through theoretical analysis, we validate the numerical simulation and introduce a new approach to study the interaction of different-order modes of polaritons.

This phenomena observed in twisted β -Ga₂O₃ slabs enables us to manipulate the longitudinal attenuation characteristics of polaritons at fixed frequency points and material thickness, opening a new dimension for optical field control within sub-wavelength scales.

Our research, involving the fusion of polaritons of varying orders and decaying characteristics, can inspire new directions for polariton studies with promising applications in integrated photonics and nano-optics. Additionally, the introduction of novel interlayer electron wavefunction interactions could inspire the design of advanced nanostructures, such as innovative heterostructures.

Data Availability

The data supporting our study is available from the corresponding author upon reasonable request.

Received: 5 November 2024; Accepted: 15 January 2025; Published online: 06 March 2025

References

- Basov, D. N., Fogler, M. M. & de Abajo, F. J. G. Polaritons in van der Waals materials. Science 354, aag1992 (2016).
- Dai, S. et al. Tunable Phonon Polaritons in Atomically Thin van der Waals Crystals of Boron Nitride. Science 343, 1125–1129 (2014).
- 3. Huang, K. U. N. Lattice vibrations and optical waves in ionic crystals. *Nature* **167**, 779–780 (1951).
- Low, T. et al. Polaritons in layered two-dimensional materials. *Nat. Mater.* 16, 182–194 (2017).
- 5. Ma, W. et al. In-plane anisotropic and ultra-low-loss polaritons in a natural van der Waals crystal. *Nature* **562**, 557–562 (2018).
- 6. Voronin, K. V. et al. Fundamentals of polaritons in strongly anisotropic thin crystal layers. *Acs Photonics* **11**, 550–560 (2024).
- 7. Wang, C. et al. Van der Waals thin films of WTe2 for natural hyperbolic plasmonic surfaces. *Nat. Commun.* **11**, 1158 (2020).
- Xie, Y. A. et al. Tunable optical topological transitions of plasmon polaritons in WTe van der Waals films. *Light Sci. Appl.* 12, 193 (2023).

- Taboada-Gutiérrez, J. et al. Broad spectral tuning of ultra-low-loss polaritons in a van der Waals crystal by intercalation. *Nat. Mater.* 19, 964–968 (2020).
- Sun, T. et al. Van der Waals quaternary oxides for tunable low-loss anisotropic polaritonics. Nat. Nanotechnol. 19, 758–765 (2024).
- Autore, M. et al. Boron nitride nanoresonators for phonon-enhanced molecular vibrational spectroscopy at the strong coupling limit. *Light Sci. Appl.* 7, 17172 (2018).
- Lv, J. T. et al. Hyperbolic polaritonic crystals with configurable lowsymmetry Bloch modes. Nat. Commun. 14, 3894 (2023).
- Tresguerres-Mata, F. A. I. et al. Observation of naturally canalized phonon polaritons in LiV2O5 thin layers. Nature. *Communications* 15, 2696 (2024).
- Alvarez-Perez, G. et al. Infrared permittivity of the biaxial van der Waals semiconductor α-MoO from near- and far-field correlative studies. Adv. Mater. 32 (2020).
- Giles, A. J. et al. Ultralow-loss polaritons in isotopically pure boron nitride. *Nat. Mater.* 17, 134–139 (2018).
- Li, P. et al. Optical Nanoimaging of hyperbolic surface polaritons at the edges of van der Waals materials. Nano Lett. 17, 228–235 (2017).
- Ma, W. L. et al. Ghost hyperbolic surface polaritons in bulk anisotropic crystals. *Nature* 596, 362–366 (2021).
- 18. Hu, G. et al. Topological polaritons and photonic magic angles in twisted α -MoO3 bilayers. *Nature* **582**, 209–213 (2020).
- Zhao, Y. et al. Ultralow-Loss Phonon Polaritons in the Isotope-Enriched α-MoO3. Nano Lett. 22, 10208–10215 (2022).
- Alexeev, E. M. et al. Resonantly hybridized excitons in moire superlattices in van der Waals heterostructures. *Nature* 567, 81–86 (2019).
- Hu, G. W. et al. Moire hyperbolic metasurfaces. Nano Lett. 20, 3217–3224 (2020).
- Duan, J. et al. Multiple and spectrally robust photonic magic angles in reconfigurable α-MoO3 trilayers. Nat. Mater. 22, 867–872 (2023).
- 23. Alvarez-Pérez, G. et al. Active tuning of highly anisotropic phonon polaritons in Van der Waals crystal slabs by gated graphene. *ACS Photonics* **9**, 383–390 (2022).
- Zeng, Y. L. et al. Tailoring topological transitions of anisotropic polaritons by interface engineering in biaxial crystals br. *Nano Lett.* 22, 4260–4268 (2022).
- Gomez-Diaz, J. S., Tymchenko, M. & Alù, A. Hyperbolic plasmons and topological transitions over uniaxial metasurfaces. *Phys. Rev. Lett.* 114, 233901 (2015).

- Carr, S. et al. Twistronics: manipulating the electronic properties of two-dimensional layered structures through their twist angle. *Phys. Rev. B* 95, 075420 (2017).
- Duan, J. H. et al. Twisted nano-optics: manipulating light at the nanoscale with twisted phonon polaritonic slabs. *Nano Lett.* 20, 5323–5329 (2020).
- Sheinfux, H. H. & Koppens, F. H. L. The rise of twist-optics. *Nano Lett.* 6935–6936 (2020).
- Zheng, Y. et al. Hyperbolic transition of phonon polaritons from volume to surface modes in β-Ga2O3. J. Opt. Soc. Am. B https://doi. org/10.1364/JOSAB.546214 (2025).
- Wang, H. W. et al. Planar hyperbolic polaritons in 2D van der Waals materials. Nat. Commun. 15, 69 (2024).
- Galiffi, E. et al. Extreme light confinement and control in low-symmetry phonon-polaritonic crystals. *Nat. Rev. Mater.* 9, 9–28 (2024).
- Dai, S. et al. Graphene on hexagonal boron nitride as a tunable hyperbolic metamaterial. *Nat. Nanotechnol.* 10, 682–686 (2015).
- 33. Hu, G. et al. Real-space nanoimaging of hyperbolic shear polaritons in a monoclinic crystal. *Nat. Nanotechnol.* **18**, 64–70 (2022).
- 34. Matson, J. et al. Controlling the propagation asymmetry of hyperbolic shear polaritons in beta-gallium oxide. *Nat. Commun.* **14**, 5240 (2023).
- 35. Passler, N. C. et al. Hyperbolic shear polaritons in low-symmetry crystals. *Nature* **602**, 595–600 (2022).
- Álvarez-Pérez, G. et al. Analytical approximations for the dispersion of electromagnetic modes in slabs of biaxial crystals. *Phys. Rev. B* 100, 235408 (2019).
- Dai, Z. G. et al. Edge-oriented and steerable hyperbolic polaritons in anisotropic van der Waals nanocavities. *Nat. Commun.* 11, 6086 (2020)
- Zhang, Q. et al. Hybridized hyperbolic surface phonon polaritons at α-MoO3 and polar dielectric interfaces. Nano Lett. 21, 3112–3119 (2021).
- 39. Ruta, F. L. et al. Surface plasmons induce topological transition in graphene/α-MoO3 heterostructures. *Nat. Commun.* **13**, 3719 (2022).
- Gonçalves, P. A. D. et al. Strong light–matter interactions enabled by polaritons in atomically thin materials. *Adv. Opt. Mater.* 8, 1901473 (2020).
- Conrads, L. et al. Direct programming of confined surface phonon polariton resonators with the plasmonic phase-change material In3SbTe2. Nat. Commun. 15, 3472 (2024).
- Caldwell, J. D. et al. Sub-diffractional volume-confined polaritons in the natural hyperbolic material hexagonal boron nitride. *Nat. Commun.* 5, 5221 (2014).
- 43. Dai, S. et al. Subdiffractional focusing and guiding of polaritonic rays in a natural hyperbolic material. *Nat. Commun.* **6**, 6963 (2015).
- Zheng, C. Q. et al. Molding broadband dispersion in twisted trilayer hyperbolic polaritonic surfaces. Acs Nano 16, 13241–13250 (2022).

Acknowledgements

This work is supported by National Natural Science Foundation of China (Grant Nos. 12361161667 and 12374410), National Key Research and Development Program of China (Grant Nos. 2020YFA0710100 and 2023YFA1407100), Fundamental Research Funds for the Central Universities (Grant No. 20720240152).

Author contributions

Y.Z. (Yuan Zheng) derived the theoretical model, performed the numerical simulation and wrote the manuscript. Y.Z. (Yali Zeng) and H.C. reviewed and revised the manuscript. All authors revised the figures and adjusted the format of the manuscript.

Competing interests

The authors declare no competing interests.

Additional information

Supplementary information The online version contains supplementary material available at https://doi.org/10.1038/s44310-025-00053-w.

Correspondence and requests for materials should be addressed to Huanyang Chen.

Reprints and permissions information is available at http://www.nature.com/reprints

Publisher's note Springer Nature remains neutral with regard to jurisdictional claims in published maps and institutional affiliations.

Open Access This article is licensed under a Creative Commons Attribution-NonCommercial-NoDerivatives 4.0 International License, which permits any non-commercial use, sharing, distribution and reproduction in any medium or format, as long as you give appropriate credit to the original author(s) and the source, provide a link to the Creative Commons licence, and indicate if you modified the licensed material. You do not have permission under this licence to share adapted material derived from this article or parts of it. The images or other third party material in this article are included in the article's Creative Commons licence, unless indicated otherwise in a credit line to the material. If material is not included in the article's Creative Commons licence and your intended use is not permitted by statutory regulation or exceeds the permitted use, you will need to obtain permission directly from the copyright holder. To view a copy of this licence, visit https://creativecommons.org/licenses/by-nc-nd/4.0/.

© The Author(s) 2025